Int. J. Electrochem. Sci., 10 **(2015)** 9652 - 9665

International Journal of
ELECTROCHEMICAL
SCIENCE
www.electrochemsci.org

Lithium Storage Characteristics and Electrochemical Performance of Si-Sb-Ag Composite Anode Materials

Yang Wang, Peixin Zhang[*]*, Jingwei Wang, Yongliang Li*[*]*, Xiangzhong Ren*

School of Chemistry and Environmental Engineering, Shenzhen University, Shenzhen 518060, PR China
[*]E-mail: pxzhang@szu.edu.cn, liyli@szu.edu.cn

Received: 31 July 2015 / *Accepted:* 8 September 2015 / *Published:* 30 September 2015

Si-Sb-Ag composite anode materials are synthesized by a chemical reduction-mechanical alloying (MA) method. Their microstructures, morphologies and electrochemical properties are characterized by X-ray diffraction (XRD), field-emission scanning electron microscopy (FE-SEM), galvonostatic charge/discharge tests, cyclic voltammetry (CV) and electrochemical impedance spectroscopy (EIS). The results indicate that Ag is uniformly dispersed in Si-Sb immiscible alloy and the conductivity of the composite is increased. Moreover, Ag exhibits high ductility which efficiently improves the cycle performance by reducing the shredding and powdering of anode materials during the volume expansion. Electrochemical results show that $Si_{0.8}SbAg_{0.4}$ exhibits the best electrochemical performance with an initial discharging capacity of 1405.6 mAh g^{-1} and 638.7 mAh g^{-1} after 50 cycles. The cycle life of $Si_{0.8}$Sb-Ag composite anodes could be improved by adjusting the charge/discharge voltage range, which controlled the lithiation degree of Ag and reduced the lithiation degree of silicon.

Keywords: lithium-ion batteries; anode materials; $Si_{0.8}$Sb-Ag composite material; composite materials; electrochemical performance

1. INTRODUCTION

The Si-based alloy anode materials have been the one of the most promising anode materials for lithium ion batteries (LIBs) due to the high energy capacity, good conductivity, environmental compatibility and low cost. Recently, studies are mainly performed on the Si-M binary system, which M is another metal element (M=Cr[1], Ge[2], Ti[3], Fe[4], Ni[5], Ti[6], Sn[7], Al[8], Ag[9], Cu [10] and Sb[11]). Nevertheless, the Si-based alloy particles lose electrical contact with each other because of the huge volume expansion during charge/discharge processes. The shredding and powdering of alloy particles reduce the electrochemical activity, which hinders the transport for electrons and Li^+,

resulting in poor cycle stability and large capacity attenuation. The discharge capacity of Si-based composites can be improved by reducing the grain size to nanoscale which decreases the diffusion distance for lithium ions [12-14]. However, the nanoscale materials are easily agglomerated and reunited when the grain size is less than 100 nm which causes the decreasing of cycle performance [15, 16]. Therefore, improving the cycle stability as well as maintaining the high capacity has currently been an attractive research area in Si-based anode materials.

In our previous research, the immiscible $Si_{0.8}Sb$ alloy was synthesized by a chemical reduction-mechanical alloying (MA) method and was demonstrated moderate electrochemical and cycle performance with a reversible capacity of 596.4 mAh g^{-1}. There was no traditional intermetallic and solid solution phase in this system, which means that Si and Sb exist as simple substance phases [11]. And the components in the system were refined into nanoscale and homogeneously dispersed, forming a nanophase composite structure [17-19]. The buffering matrices of Li_xSi and Li_xSb interacted with each other and consequently the volume expansion was suppressed, which significantly improve the discharge capacity and the cycle performance.

Studies on Sn-Sb-Ag composite anode materials indicate that the introduction of Ag could reduce the crystallization degree and the powdering of the parent immiscible alloy phase during the lithium storage process [20, 21]. Due to its good conductivity and ductility, Ag serves as a conductive medium for both lithium ions and electrons, resulting in good cycle performance after cycling [22, 23]. Researches have also indicated that $Li_8Si_5Ag_3$ formed during the lithiation process can improve the cycle performance of Si-based materials [24]. Therefore, this paper proposes using a ternary Si-Sb-Ag composite system to obtain excellent performance.

2. EXPERIMENTAL

2.1 Preparation and characterization

All of the reagents were of analytical grade and used without further purification. Distilled water was used in all experiments. Nano-sized composite powders were synthesized by a chemical reduction-MA method in this study. Typically, 5 ml of $AgNO_3$ solutions with different concentrations were added drop wise to a 0.2 M $NaBH_4$ aqueous solution, respectively while the amount of $NaBH_4$ were excess to ensure a complete reduction of the metal ions. Then 100 mL of 0.1 M $SbCl_3$ ethanol was immediately added into the above solutions with vigorous magnetic stirring at room temperature. After 30 min stirring, the mixtures were aged in a water bath at 80 ℃ for 5 h. The solutions were filtered, and the products were washed thoroughly using distilled water and ethanol. And high-energy ball milling was applied for the MA processes. All steps prior to milling were conducted inside an Ar-filled glove box. The elemental Si, Sb and Ag powders were mixed at a mole ratio of 4:5: *x* with ethanol as solvent and loaded into a 100 ml stainless steel vial. The milling was performed under argon atmosphere for 15 h and the products were dried at 120 ℃ for 10 h under vacuum. The final products were sifted with a 200-mesh sieve and then store in the Ar-filled glove box.

The phases of the alloy powders obtained were identified using a Bruker D8 Advance X-ray diffraction (XRD) instrument. The microstructure and morphology of the particles were observed using Hitachi S-4800 and Hitachi SU-70 field-emission scanning electron microscopy (FE-SEM) instruments.

2.2 Assembling and testing

To evaluate their electrochemical characteristics, electrodes were prepared by mixing 70 wt% active materials, 10 wt% carbon black and 20 wt% polyvinylidene fluoride (PVDF) binder in 1-methy1-2-pyrrolidinone (NMP) to form a slurry, which was then spread onto a copper grid. After coating, the film was dried at 120 ℃ for 10 h under vacuum and then annealed in a furnace at 230 ℃ for 10 h.

Electrochemical measurements were performed using CR2032 coin cells assembled in the argon-filled glove box; the cells were composed of a metallic lithium foil as the counter electrode, 1 M $LiPF_6$ in ethylene carbonate (EC)-dimethyl carbonate (DMC) (1:1 v/v) as the electrolyte, Celegard 2400 as the separator and the as-synthesized alloy composites as the working electrodes. Cyclic voltammetry (CV) and electrochemical spectroscopy (EIS) were performed using a CHI660A electrochemical testing system in the range of 0-2.0 V (vs. Li/Li^+) at a scan rate of 0.02 mV s^{-1}, with a frequency of 10^5-10^{-2} Hz and amplitude of 5 mV.

3. RESULTS AND DISCUSSION

3.1 Phase structures and morphologies

Fig. 1 shows the XRD patterns of $Si_{0.8}SbAg_x$ composites obtained by chemical reduction-MA method. As shown in the picture, the diffraction patterns of the composites contain sharp Si, Sb and weak Ag peaks, indicating that there is no intermetallic compound formed by this method and Ag nanoparticles disperses evenly in the immiscible $Si_{0.8}Sb$ matrices. The crystallinity of the anode materials is decreased with the mechanical alloying. The characteristic peak intensities of Si, Sb and Ag are gradually increased with the increase of the Ag contents. Additionally, the peak of Ag was broadening which could be attributed to partial amorphization. The formation of an amorphous phase by mechanical alloying has been described in the Cu-Ta system, which is characterized by a positive heat of mixing. Further study was underway to examine more details of the microstructure by transmission electron microscope.

Fig. 2 shows FE-SEM images of the $Si_{0.8}SbAg_{0.4}$ composite. The composite is composed of tiny irregular particles, which gathers into homogenous secondary particles without distinct agglomeration (Fig. 2a). A back-scattered image of $Si_{0.8}SbAg_{0.4}$ composite is shown in Fig. 2b, Si, Sb and Ag are integrated and show little difference among different phases, leading to an inconspicuous difference in atomic number/composition contrast.

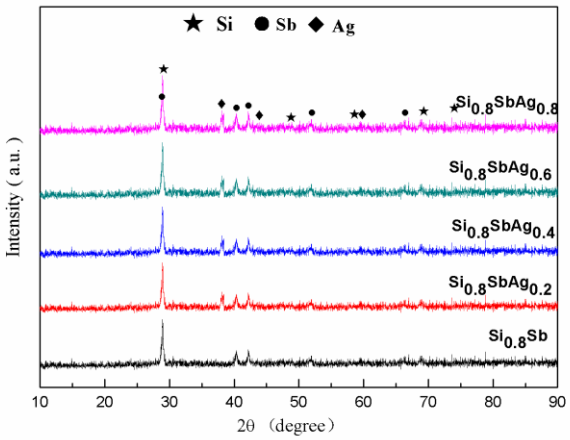

Figure 1. XRD patterns of the $Si_{0.8}SbAg_x$ composite materials.

Fig. 2c shows the EDX analysis results and element mapping of $Si_{0.8}SbAg_{0.4}$, indicating that the composite consists of Si (36.17 at%), Sb (45.55 at%) and Ag (18.28 at%), i.e., Si (12.48 wt%), Sb (63.24 wt%) and Ag (24.28 wt%), which are close to the theoretical values.

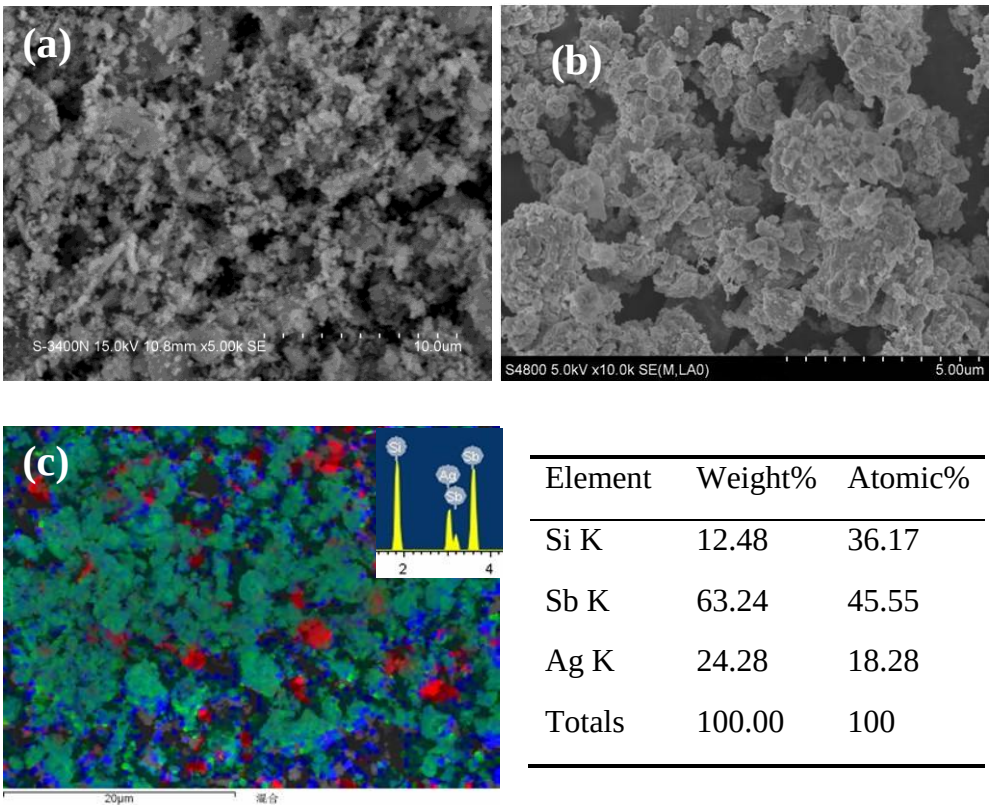

Element	Weight%	Atomic%
Si K	12.48	36.17
Sb K	63.24	45.55
Ag K	24.28	18.28
Totals	100.00	100

Figure 2. (a) FE-SEM image of $Si_{0.8}SbAg_{0.4}$; (b) back-scattered image of $Si_{0.8}SbAg_{0.4}$; (c) energy spectrum analysis and element mapping of $Si_{0.8}SbAg_{0.4}$ (Si-red, Sb-green, Ag-blue).

It can be concluded that an immiscible Si-Sb system formed in which most Si is clad by Sb and a small amount of bare Si appears on the surface of the immiscible alloy [11]. There is no traditional intermetallic compound formed but a novel Si-Sb-Ag composite, in which Ag disperses uniformly in the Si-Sb immiscible alloy.

Fig. 3 shows conductivity versus Ag content curves describing the relationship between electrical conductivity and Ag content in $Si_{0.8}SbAg_x$. When Ag contents are 0, 0.2, 0.4, 0.6 and 0.8, the conductivity values are 0.42, 2.83, 6.69, 10.55 and 17.32 S cm^{-1}, respectively. The conductivity increases with the addition of Ag, it is expected that the electrochemical performance of the immiscible Si-Sb alloy system can be improved by the introduction of Ag.

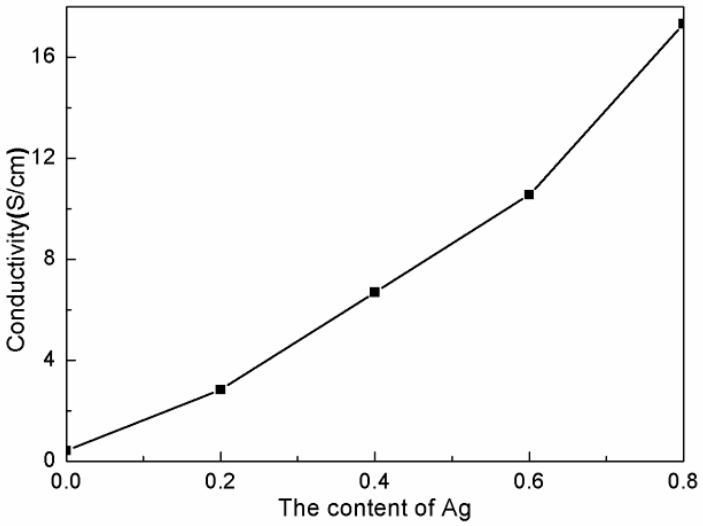

Figure 3. Conductivity versus Ag content curves of $Si_{0.8}SbAg_x$ composites.

3.2 Electrochemical properties of $Si_{0.8}SbAg_x$ composite anode materials

The cycle performance of $Si_{0.8}SbAg_x$ composite anode materials between 0 and 2 V for 50 cycles is plotted in Fig. 4. The initial specific capacities of $Si_{0.8}SbAg_x$ (x=0,0.2, 0.4, 0.6 and 0.8) are 1288.4, 1312.6, 1405.6, 1388.9 and 1276.5 mAh g^{-1}, and are 596.4, 604.8, 638.7, 560.1 and 553.0 mAh g^{-1} after 50 cycles, demonstrating that the appropriate addition of Ag significantly affects the capacity. Nonetheless, Elemental Ag is easily nucleated into large particles and impedes the contact between active particles, resulting in shredding of the active grains and collapsing of the porous structure during cycles. Among different Ag contents, $Si_{0.8}SbAg_{0.4}$ composite exhibits the best electrochemical performance with the capacity retention of 63.12%. These results suggest that the good ductility and flexibility of Ag can effectively relieve the volume expansion of the composite electrode and thus improve the cycle performance. Moreover, due to its high conductivity, Ag also serves as a conducting medium and infinitely promotes the electronic and ionic conduction, therefore improving the discharging capacity of the composite materials.

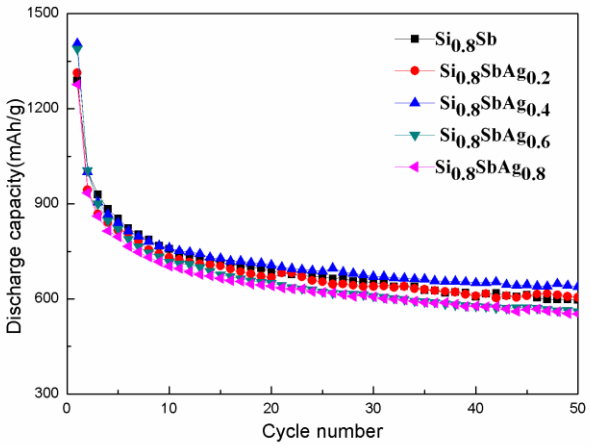

Figure 4. Cycle performance of $Si_{0.8}SbAg_x$ composite anode materials.

Fig. 5 shows the electrochemical impedance of $Si_{0.8}SbAg_x$ (x=0, 0.2, 0.4, 0.6, 0.8) composite anodes and the fitting results before cycling. It can be seen that all the plots composed of semicircles with a large radius of curvature and sloping lines. The radius at the high-frequency increase with Ag content, and the linear slopes component at low frequency show little change. The semicircle in the high-frequency intercept represents as the contact resistance without lithium insertion, charge transfer and lithium-ion diffusion at the open voltage. The inset of Fig. 5 shows the impedance responses, which were then analyzed using an equivalent circuit that takes into account all possible contributions to the impedance of the test cell, using resistance *R*s as the electrolyte impedance, *Q*g as the diffusive resistance and *Q*cf and *R*cf as the contact resistances. All of the equivalent circuits were fit very well with the experimental data, and the representative fitting results are shown in Table 1. As can be seen, the appropriate addition of Ag decreases aggregation in the immiscible Si-Sb system, while promotes electrolyte infiltration and maintains the high conductivity and ductility of Ag. And the diffusion and transmission of lithium ions are enhanced and active particles are prevented from powdering and shredding. Consequently, the electrode structure is maintained and the contact resistance is reduced.

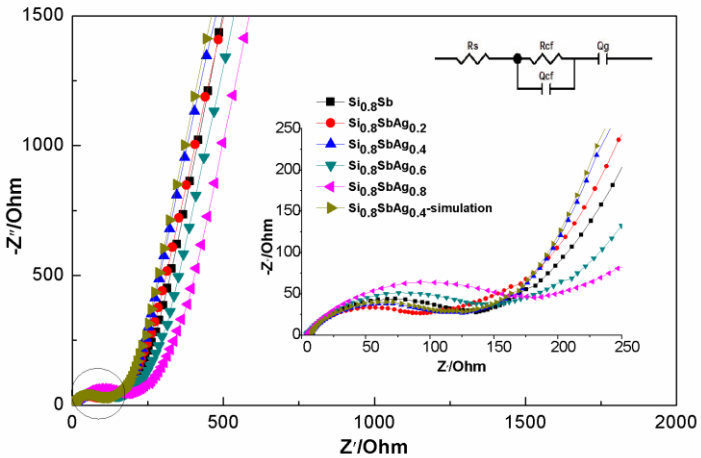

Figure 5. EIS of $Si_{0.8}SbAg_x$ at the open voltage.

Table 1. Impedance parameters of the $Si_{0.8}SbAg_x$ composite materials before cycling.

	Rs/*Ω*	*Rcf*/*Ω*	***Q***g/***F***
$Si_{0.8}Sb$	4.68	138.5	0.002743
$Si_{0.8}SbAg_{0.2}$	4.35	104.6	0.002089
$Si_{0.8}SbAg_{0.4}$	4.29	101.3	0.001958
$Si_{0.8}SbAg_{0.6}$	4.70	146.5	0.002936
$Si_{0.8}SbAg_{0.8}$	4.73	163.6	0.003565

Fig. 6 shows the cycle performance of $Si_{0.8}SbAg_{0.4}$ under different current densities over the voltage range of 0-2.0 V. When the current densities are 50, 100 and 200 μA/cm^2, the initial specific capacities are 1260.5, 1405.6 and 1237.7 mAh g^{-1} and are 620.1, 638.7 and 599.4 mAh g^{-1} after 50 cycles. The capacity remains high with a lower current density because the electrode is fully lithiated. A lower current density can also delay the electrolyte decomposition and the SEI film formation, leading to better contact between active particles and electrolyte. By contrast, the electrochemical and concentration polarization are pronounced for the reason that reactions on the surface of the electrode proceed to a higher extent at a higher current density. The increased internal impedance hinders the lithium-ions from transporting into the active materials, resulting in a capacity decrease. When the density is 100 μA/cm^2, the electrode exhibits the best electrochemical properties due to an appropriate reaction rate, with which the timely formation of SEI film and fully lithiated/de-lithiated. All of these results indicate that the current density affects not only on the charge/discharge efficiency but also on the utilization of the active particles.

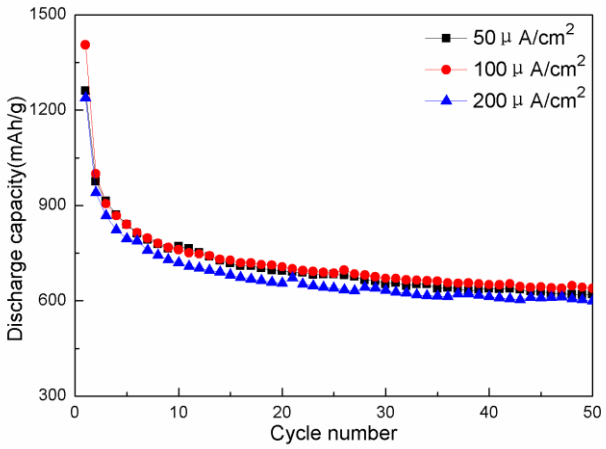

Figure 6. Cycle performance of $Si_{0.8}SbAg_{0.4}$ under different current densities.

Fig. 7 shows the cycle performance of the $Si_{0.8}SbAg_{0.4}$ anode material over different operating voltage ranges. When the cutoff voltages are 0, 0.03, 0.05 and 0.1 V, the corresponding initial discharging capacities are 1405.6, 1313.2, 1158.2 and 970.6 mAh g^{-1}, respectively. The initial discharge specific capacity decreases along with the increase of the discharge cutoff voltage because the lithiation potential of Si is lower during the initial cycle. The discharging specific capacities are

638.7, 612.0, 550.7 and 485.9 mAh g^{-1} after 50 cycles with the capacity retention of 63.13, 66.42, 63.68 and 64.67%, respectively. When the cutoff voltage was 0 V, the lithiation degree of Ag was higher and the porous structure was destroyed, leading to a low reversible capacity retention and poor cycle performance. When the cutoff voltage was 0.03 V, the lithiation of Ag was weakened and the volume expansion was buffered by formation of $SbLi_3$ as the buffering matrix, thereby achieving stable cycle performance. When the cutoff voltage was 0.1 V, although the volume expansion was reduced, the deep lithiation of Si and the activating reaction were affected by the lower discharging capacity, which resulted in a low capacity during later cycles. The results indicate that the composite anodes cycled within a limited voltage range exhibit much better cycle life than those cycled over the full voltage range, which affects the capacity of the anode materials. The cycling stability can be improved by restricting either the upper or lower cutoff voltage and weakening the depth of the lithium extraction-insertion, which can reduce the volume expansion and the destruction due to strain and promote the activity of lithium intercalation/de-intercalation. Since the alloying process between Li and Ag requires a low potential to generate Li_xAg ($1 \leq x \leq 4$) [24-27], the cycle stability can be improved by controlling either the upper or cutoff potential, which can weaken the degree of lithiation of Ag and maximize its flexibility, ductility, conductivity, therefore, playing an important role as a buffering matrix.

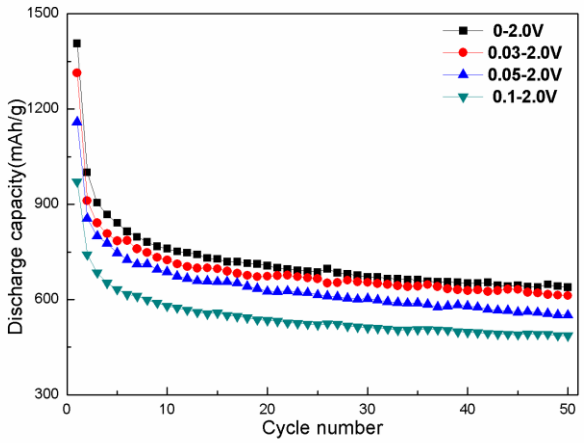

Figure 7. Cycle performance of $Si_{0.8}SbAg_{0.4}$ over different operating voltage ranges.

3.3 Analysis of lithium intercalation characteristics and interface structure

Fig. 8 shows the initial charge-discharge curves of the $Si_{0.8}SbAg_x$ anode materials over the operating voltage range of 0-2.0 V. The trends of the curves are similar, showing that the increase of the Ag content does not affect the mechanism of lithium extraction and insertion. The initial discharging curves are composed of four parts, with two main discharge platforms and a narrow discharge platform. The first part is a decrease above 0.8 V, where the voltage drops rapidly corresponding to irreversible reactions such as the reduction of oxides on the electrode, electrolyte decomposition and the formation of SEI films. The ductility of Ag reduces its destruction due to volume expansion. $Si_{0.8}SbAg_{0.4}$ exhibits the best electrochemical properties, though the performance

decreases with increasing Ag content. The second part is a potential plateau from 0.8 to 0.65 V; the following reduction reaction is proposed: $Si_xSb+3Li^++3e^-\rightarrow Li_3Sb+xSi$, which is likely due to the Li intercalation of Si_xSb to form Li_3Sb. Due to the rock-salt structure and lattice symmetry (R-3m) of the anode, Sb occupies the center when it is embedded by lithium and forms a stable face-centered cubic structure, while Li occupies the Td sites and Oh sites [26]. The third part is the region from 0.4-0 V. Upon discharging, the composite shows a series of small and narrows steps, which correspond to Si reacting with Li to form various Li_xSi compounds, particularly below 0.2 V. A small amount of Ag reacts with Li to form Li_xAg below 0.1 V. As a matrix, Li_3Sb can effectively restrain the volume expansion of Si, boost the intercalation depth and promote the utilization of active particles. Si and Sb serve as matrices for each other and compensate for their relative volume expansion during the lithium intercalation process. Moreover, the good flexibility, ductility and conductivity of Ag improve the electrochemical properties and cycle performance of the anode materials.

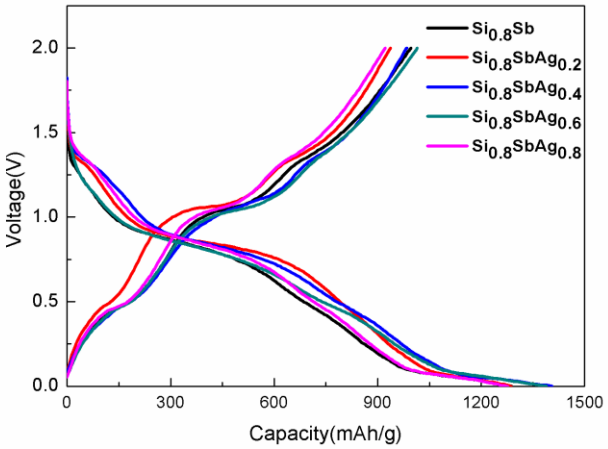

Figure 8. The initial charging/discharging curves of $Si_{0.8}SbAg_x$ anode material.

Fig. 9 shows the charging-discharging curves of the $Si_{0.8}SbAg_{0.4}$ anode material after 1st, 2nd, 10th, 20th, 30th, 40th and 50th cycles over the voltage range of 0-2.0 V. The results show a similar trend, but the capacities decrease over subsequent cycles which are due to the powdering and shredding of anode materials and hinder lithium-ion from becoming trapped in the active materials. However, after the first 10 cycles, the internal and interfacial structures of electrode materials become stable since the volume expansion are restricted by the buffering matrix, and the capacity decays slowly over later cycles.

Fig. 10 shows SEM images of the morphology of the $Si_{0.8}SbAg_{0.4}$ composite electrodes before/after cycling. As shown in Fig. 10a, the active materials are dispersed uniformly on the surface of the electrode and contact with each other closely, which allows electrolyte absorption and electron transport. Fig. 10b shows that the electrode is covered by a dense SEI film after 2th cycles; the surface of the electrode shows a rugged morphology due to volume expansion and particles penetrating the surface of the electrode.

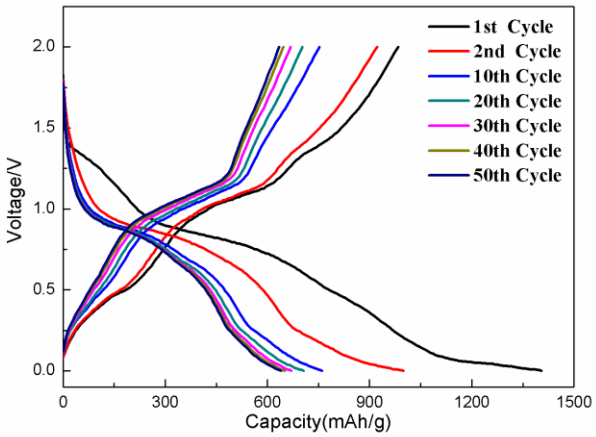

Figure 9. Charging/discharging curves of $Si_{0.8}SbAg_{0.4}$ anode after 1st, 2nd, 10th, 20th, 30th, 40th and 50th cycles.

Meanwhile, Fig. 10c shows that the surface of the electrode cracks and the active particles shred and powder to create a smooth surface after 10th cycles. As shown in Fig. 10d, the morphology changes slightly after 50th cycles and the formed layered structure reduces the length for lithium-ion and electron transport and reduces the capacity attenuation in later cycles.

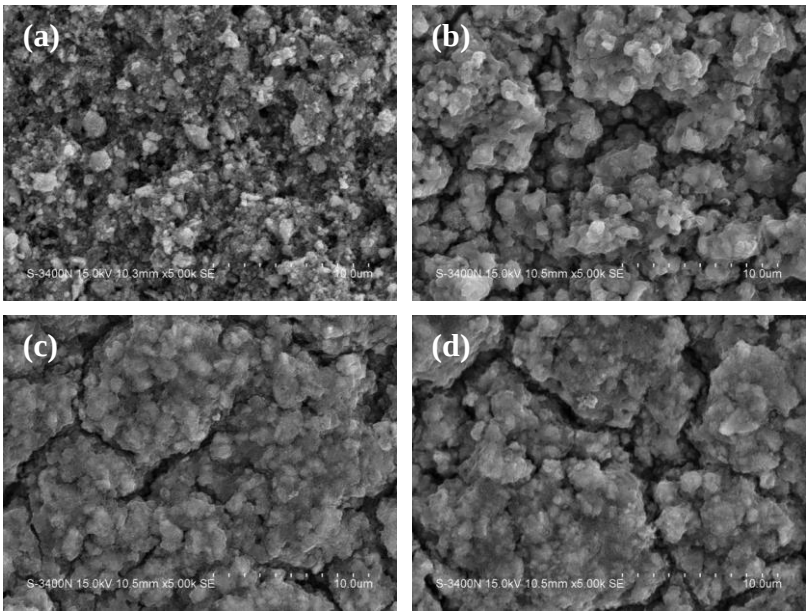

Figure 10. SEM images of the $Si_{0.8}SbAg_{0.4}$ composite anode: (a) before cycling, (b) after 2th cycles, (c) after 10th cycles and (c) after 50th cycles.

Fig. 11 shows the CV curves for the $Si_{0.8}SbAg_x$ composite anode materials. Results show that although Ag reacts with lithium at low voltage, it has negligible effects on the lithiation degree. The curves have similar shapes, indicating that the addition of Ag does not change the lithium/de-lithium

cutoff point. However, excessive Ag will result in large particles and a decrease in capacity. For the cathodic scan, a series of weak reduction peaks are observed in the first cycle at 1.35 V and do not appear in subsequent cycles, indicating that the process involves one or more irreversible reduction reactions. It is mainly due to the irreversible lithiation of Sb-oxides that generated in synthesis and annealing processes [28]. Moreover, the CuO film formed in open air was easily converted to Cu_2O, which reacted with lithium irreversibly in an inert gas [29]. A sharp peak appears between 1.0 V and 0.7 V, corresponding to Li insertion into Sb and the formation of the Li_3Sb alloy. A series of peaks observed around 0.45 V correspond to lithiation processes with both native and extruded Si materials, generating $Li_{0\text{-}1.7}Si$, $Li_{1.71\text{-}2.33}Si$, $Li_{2.33\text{-}3.25}Si$ and $Li_{3.75\text{-}4.2}Si$ [30-32]. Another series of weak reduction peaks weaken or disappear in subsequent cycles, indicating that the processes involve irreversible reduction reactions such as the decomposition of the electrolyte, the irreversible phase process of silicon and the shredding and inactivation of active particles. The anodic scan shows sharp oxidation peaks at 0.32, 0.46, 0.97, 1.07, 1.1 and 1.38 V (vs. Li/Li^+), which propagate through subsequent cycles with a stable peak intensity; these peaks correspond to the extraction of lithium from the Li_3Sb and Li_xSi materials respectively and demonstrate the excellent stability of the composites.

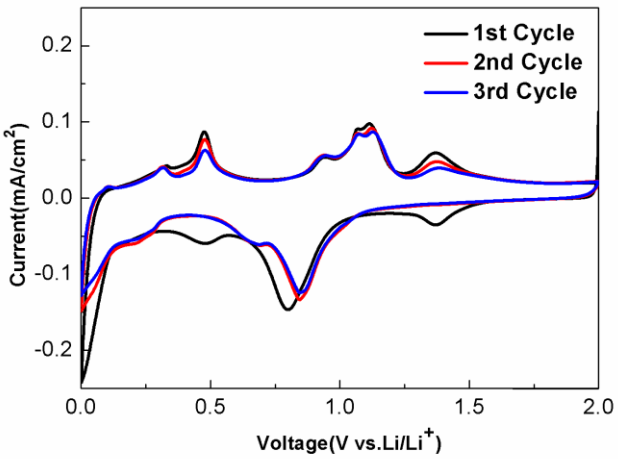

Figure 11. CV curves of $Si_{0.8}SbAg_x$ composite materials.

Fig. 12 compares the impedance response of $Si_{0.8}SbAg_x$ and the representative fitting results after the first lithium insertion-extraction cycles. The radius of the semicircles in the low-frequency are observed to increase as the number of cycles increases for the reason that the generated Li_xSb, Li_xSi and Li_xAg packed the active particles and blocked the transport channels for lithium and electrons, resulting in an increase in the impedance. During de-lithiation, which is actually de-alloying, the composites decomposed, recovering the porous electrode structure and unblocking the channels; therefore, the internal impedance decreased.

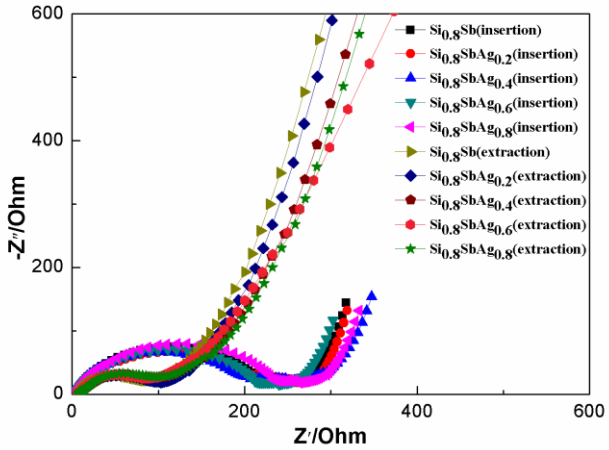

Figure 12. EIS of $Si_{0.8}SbAg_x$ composite anode materials after the initial cycle.

Fig. 13 shows the EIS of the $Si_{0.8}SbAg_{0.4}$ composite material. The results show that with increasing cycle number, the radii of the high-frequency semicircles and the internal impedance increase. Although the conductivity and the ductility of the electrode were promoted by Ag, the porous structure collapses due to the powdering and shredding of active particles with increasing cycle number. The shredded powders covered the surface of the anode and prevented lithium ions from becoming trapped in the active electrode materials, leading to an increase in the interfacial and internal resistance and ultimately poor electrochemical activities and stability.

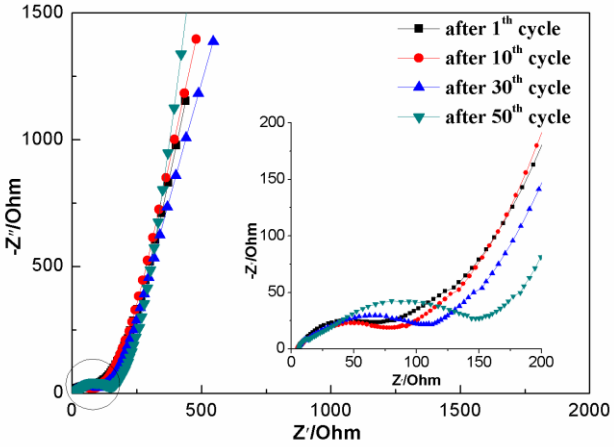

Figure 13. EIS of $Si_{0.8}SbAg_{0.4}$ anode material after different cycles.

4. CONCLUSIONS

In conclusion, Si-Sb-Ag composite materials were synthesized by a chemical reduction-mechanical alloying method and Ag was uniformly dispersed in Si-Sb immiscible system. The

addition of Ag effectively improved the conductivity of the composite materials; moreover, the good ductility of Ag helps buffering the volume expansion and reducing the shredding of active particles and structural changes, thereby promoting the cycle properties.

When the Ag content was 0.4, the initial discharging specific capacity is 1405.6 mAh g^{-1} and after 50 cycles was 638.7 mAh g^{-1}, which indicated a good electrochemical properties. The Si-Sb-Ag composite anode exhibited excellent cycle life by controlling the charging/discharging voltage range, which reduced the lithiation degree of Ag. When the voltage ranges was 0.03-2.0 V, the composite material exhibited excellent cycle performance. Current density affected the electrochemical properties and charging/discharging efficiency of the composites. When the density was 100 $\mu A/cm^2$, the electrochemical and concentration polarization were weakened and the lithium/de-lithium depth as well as the utilization of the active particles were increased. Accordingly, the discharging capacity and the operating efficiency of the resulting battery were improved.

ACKNOWLEDGEMENTS
This work was financially supported by the National Natural Science Foundation of China (Grant#51374146, 50874074), Shenzhen Government's Plan of Science and Technology (Grant #JCYJ20120613173950029).

References

1. M. Fleischauer, J. Topple, J. Dahn, *Electrochem. solid-state lett.* 8 (2005) A137.
2. T. Křenek, N. Murafa, P. Bezdička, J. Šubrt, J. Pola, *J. Anal. Appl. Pyrol.* 89 (2010) 137.
3. F. Di Quarto, F. Di Franco, C. Monarca, M. Santamaria, H. Habazaki, *Electrochim. Acta* 110 (2013) 517.
4. J.-A. Choi, D.-W. Kim, Y.-S. Bae, S.-W. Song, S.-H. Hong, S.-M. Lee, *Electrochim. Acta* 56 (2011) 9818.
5. S.M. Jeon, J.J. Song, S.-I. Kim, H.J. Kwon, K.Y. Sohn, W.-W. Park, *Met. Mater. Int.* 19 (2013) 27.
6. Y.H. Wang, Y. He, R.J. Xiao, H. Li, K.E. Aifantis, X.J. Huang, *J. Power Sources* 202 (2012) 236.
7. T. Křenek, P. Bezdička, N. Murafa, J. Šubrt, P. Duchek, J. Pola, *J. Anal. Appl. Pyrol.* 86 (2009) 381.
8. Z. Jiang, C. Li, S. Hao, K. Zhu, P. Zhang, *Electrochim. Acta* 115 (2014) 393.
9. T.D. Hatchard, J.R. Dahn, *J. Electrochem. Soc.* 152 (2005) A1445.
10. W.R. Osório, D.J. Moutinho, L.C. Peixoto, I.L. Ferreira, A. Garcia, *Electrochim. Acta* 56 (2011) 8412.
11. J. Wang, Y. Wang, P. Zhang, D. Zhang, X. Ren, *J. Alloys Compd.* 610 (2014) 308.
12. C. Tan, G. Qi, Y. Li, J. Guo, X. Wang, D. Kong, H. Wang, S. Zhang, *Int. J. Electrochem. Sci.* 8 (2013) 1966.
13. M. Su, Z. Wang, H. Guo, X. Li, S. Huang, W. Xiao, L. Gan, *Electrochim. Acta* 116 (2014) 230.
14. B. Li, Q. Zhang, C. Zhang, S. Kang, X. Li, Y. Wang, *Int. J. Electrochem. Sci.* 8 (2013) 8414.
15. B.-C. Kim, H. Uono, T. Satou, T. Fuse, T. Ishihara, M. Ue, M. Senna, *J. Electrochem. Soc.* 152 (2005) A523.
16. Z. Wang, W.H. Tian, X.H. Liu, Y. Li, X.G. Li, *Mater. Chem. Phys.* 100 (2006) 92.
17. R.Z. Hu, L. Zhang, X. Liu, M.Q. Zeng, M. Zhu, *Electrochem. Commun.* 10 (2008) 1109.
18. H. Guo, H. Zhao, X. Jia, X. Li, W. Qiu, *Electrochim. Acta* 52 (2007) 4853.
19. M. Zhu, L.Z. Ouyang, Z.F. Wu, M.Q. Zeng, Y.Y. Li, J. Zou, *Mater. Sci. Eng.: A* 434 (2006) 352.

20. Y. Wang, P. Zhang, X. Ren, G. Yi, *J. Electrochem. Soc.* 158 (2011) A1404.
21. P. Zhang, Y. Wang, J. Wang, D. Zhang, X. Ren, Q. Yuan, *Electrochim. Acta* 137 (2014) 121.
22. M.Z. Zou, J.X. Li, W.W. Wen, L.Z. Chen, L.H. Guan, H. Lai, Z.G. Huang, *J. Power Sources* 270 (2014) 468.
23. B. Yang, Z. Yang, Z. Peng, Q. Liao, *Electrochim. Acta* 132 (2014) 83.
24. S.-M. Hwang, H.-Y. Lee, S.-W. Jang, S.-M. Lee, S.-J. Lee, H.-K. Baik, J.-Y. Lee, *Electrochem. Solid-State Lett.* 4 (2001) A97.
25. F. Wang, G. Yao, M. Xu, M. Zhao, P. Zhang, X. Song, *Mater. Sci. Eng.: B* 176 (2011) 442.
26. J.T. Vaughey, L. Fransson, H.a. Swinger, K. Edström, M.M. Thackeray, *J. Power Sources* 119-121 (2003) 64.
27. J. Yin, M. Wada, S. Tanase, T. Sakai, *J. Electrochem. Soc.* 151 (2004) A867.
28. H. Bryngelsson, J. Eskhult, L. Nyholm, M. Herranen, O. Alm, *Chem. Mater.* 19 (2007) 1170.
29. J. Zhang, S. Xie, X. Wei, Y.J. Xiang, C.H. Chen, *J. Power Sources* 137 (2004) 88.
30. H. Li, X. Huang, L. Chen, G. Zhou, Z. Zhang, D. Yu, Y.J. Mo, N. Pei, *Solid State Ion.* 135 (2000) 181.
31. X. Liu, K. Xie, C.-m. Zheng, J. Wang, Z. Jing, *J. Power Sources* 214 (2012) 119.
32. G.X. Wang, J.H. Ahn, J. Yao, S. Bewlay, H.K. Liu, *Electrochem. Commun.* 6 (2004) 689.